AFRL-AFOSR-JP-TR-2017-0079

Graphene Infrared Transparent Electrode (GITE) and Thermal Enhancer for the Hybrid Energy Nanodevice

Yuan-Ron Ma
National Dong Hwa University

12/21/2016
Final Report

Air Force Research Laboratory
AF Office Of Scientific Research (AFOSR)/ IOA
Arlington, Virginia 22203
Air Force Materiel Command

REPORT DOCUMENTATION PAGE

Form Approved
OMB No. 0704-0188

1. REPORT DATE *(DD-MM-YYYY)*	2. REPORT TYPE	3. DATES COVERED *(From - To)*
18-12-2017	Final	21 Sep 2015 to 20 Sep 2016

4. TITLE AND SUBTITLE
Graphene Infrared Transparent Electrode (GITE) and Thermal Enhancer for the Hybrid Energy Nanodevice

5a. CONTRACT NUMBER

5b. GRANT NUMBER
FA2386-15-1-4116

5c. PROGRAM ELEMENT NUMBER
61102F

6. AUTHOR(S)
Yuan-Ron Ma

5d. PROJECT NUMBER

5e. TASK NUMBER

5f. WORK UNIT NUMBER

7. PERFORMING ORGANIZATION NAME(S) AND ADDRESS(ES)
National Dong Hwa University
No 1 Sec 2 Da Hsueh Rd
Shoufeng, 97401 TW

8. PERFORMING ORGANIZATION REPORT NUMBER

9. SPONSORING/MONITORING AGENCY NAME(S) AND ADDRESS(ES)
AOARD
UNIT 45002
APO AP 96338-5002

10. SPONSOR/MONITOR'S ACRONYM(S)
AFRL/AFOSR IOA

11. SPONSOR/MONITOR'S REPORT NUMBER(S)
AFRL-AFOSR-JP-TR-2017-0079

12. DISTRIBUTION/AVAILABILITY STATEMENT
A DISTRIBUTION UNLIMITED: PB Public Release

13. SUPPLEMENTARY NOTES

14. ABSTRACT
This work investigated the use of graphene nanosheets (GN) as a cost-effective replacement for platinum to form the counter-electrode (CE) in a dye-sensitized solar cell (DSSC). The GN counter-electrode properties were characterized by scanning electron microscopy (SEM), atomic force microscopy (AFM), Raman spectroscopy, X-ray photoelectron spectroscopy (XPS), energy dispersive spectroscopy (EDS), and cyclic voltammogram (CV), and the characteristics of the DSSCs based on the various CEs were analyzed using J-V measuremnts, incident monochromatic photon-to-current conversion efficiency (IPCE), and electrochemical impedance spectroscopy (EIS) measurements. This study also investigated two novel GN-based CEs for DSSCs. The results show that the DSSCs based on conventional Pt CEs yielded an efficiency of 7.32%. The GN-Pt composite CEs yielded a device efficiency of 6.35%, and the GN-Pt stacked CEs yielded an optimal efficiency of 8.54%, indicating a 16.7% improvement compared with the DSSCs based on conventional Pt CEs.
Electrolytes enhance reduction-oxidation reactions; thus, are a key component in DSSC devices. They provide dyes with electrons to enable the dyes to return from an excited state to the ground state; thereby, completing dye regeneration. Conventional DSSC electrolytes are mostly liquid-based. In this study, PMMA gel-based electrolytes were produced to enhance the stability of the electrolytes; hence, the DSSC devices.
This study first fabricated DSSC devices by adopting gelator-to-electrolyte solution volume ratios of 1:0.5, 1:1, and 1:1.5. According to the J-V measuremnts, IPCE, and electrochemical impedance analyses, the DSSC with the 1:1 gel-based electrolyte exhibited the most satisfactory properties, obtaining a device efficiency of 6.75 %. Furthermore, 0.1 M lithium bis(trifluoromethanesulphonyl)imide (LiTFSI) and 0.1 M camphorsulfonic acid (C

15. SUBJECT TERMS
Graphene, Transparent Materials, Electrodes, Plasmonic Absorption, Power and Energy

16. SECURITY CLASSIFICATION OF:			17. LIMITATION OF ABSTRACT	18. NUMBER OF PAGES	19a. NAME OF RESPONSIBLE PERSON
a. REPORT	b. ABSTRACT	c. THIS PAGE			WINDER, SHEENA
Unclassified	Unclassified	Unclassified	SAR		19b. TELEPHONE NUMBER *(Include area code)* +81-42-511-2008

Standard Form 298 (Rev. 8/98)
Prescribed by ANSI Std. Z39.18

Graphene Infrared Transparent Electrode (GITE) and Thermal Enhancer for a Hybrid Energy Nanodevice

Final Report for AOARD Grant 15IOA116

12/17/2016

PI and Co-PI information:
Prof. Yuan-Ron Ma, ronma@mail.ndhu.edu.tw, National Dong Hwa University, Department of Physics, No.1, Sec.2, Da-Hsueh Rd., Shou-Feng, Hualien 97401, Taiwan, Republic of China, Tel: +886-3-8633706, Fax: +886-3-8633690.

Prof. Wen-Bin Jian, wbjian@mail.nctu.edu.tw, National Chiao Tung University, Department of Electrophysics, 1001 University Rd., Hsinchu 300, Taiwan, Republic of China, Tel: +886-3-5712121-56159, Fax: +886-3-5725230,

Dr. Chih-Hung Tsai, cht@mail.ndhu.edu.tw, National Dong Hwa University, Department of Opto-Electronic Engineering, No.1, Sec.2, Da-Hsueh Rd., Shou-Feng, Hualien 97401, Taiwan, Republic of China, Tel: +886-3-8634199, Fax: +886-3-8634180.

Dr. Shin Mou, shin.mou.1@us.af.mil, Air Force Research Lab, Materials and Manufacturing Directorate

Period of Performance: 9/21/2015 – 9/20/2016

We investigate the use of graphene nanosheets (GN) as a cost-effective replacement for platinum to form the counter-electrode (CE) in a dye-sensitized solar cell (DSSC). The GN counter-electrode properties were characterized by scanning electron microscopy (SEM), atomic force microscopy (AFM), Raman spectroscopy, X-ray photoelectron spectroscopy (XPS), energy dispersive spectroscopy (EDS), and cyclic voltammogram (CV), and the characteristics of the DSSCs based on the various CEs were analyzed using J-V measuremnts, incident monochromatic photon-to-current conversion efficiency (IPCE), and electrochemical impedance spectroscopy (EIS) measurements. This study also investigated two novel GN-based CEs for DSSCs. The results show that the DSSCs based on conventional Pt CEs yielded an efficiency of 7.32%, those based on the GN-Pt composite CEs yielded a device efficiency of 6.35%, and those based on the GN-Pt stacked CEs yielded an optimal efficiency of 8.54%, indicating a 16.7% improvement compared with the DSSCs based on conventional Pt CEs. Helping reduction-oxidation reactions, electrolytes are a key component in DSSC devices; they provide dyes with electrons to enable the dyes to return from an excited state to the ground state, thereby completing dye regeneration. Conventional DSSC electrolytes are mostly liquid-based. In this study, PMMA gel-based electrolytes were produced to enhance the stability of the electrolytes and hence the DSSC devices. This study first fabricated DSSC devices by adopting gelator-to-electrolyte solution volume ratios of 1:0.5, 1:1, and 1:1.5. According to the J-V measuremnts, IPCE, and electrochemical impedance analyses, the DSSC with the 1:1 gel-based electrolyte exhibited the most satisfactory properties, obtaining a device efficiency of 6.75 %. Furthermore, 0.1 M lithium bis(trifluoromethanesulphonyl)imide (LiTFSI) and 0.1 M camphorsulfonic acid ($C_{10}H_{16}O_4S$) were separately added to the gel-based electrolytes. An impedance spectrum analysis and conductivity testing of the simple-model devices showed that the added LiTFSI and $C_{10}H_{16}O_4S$ were effective in increasing the conductivity of the electrolytes, enhancing the

device efficiency. In particular, the device with the 1:1+ LiTFSI gel-based electrolyte exhibited the optimal efficiency (7.28%), which was higher than that observed in the device with the liquid-based electrolyte. DSSC devices with the gel-based electrolytes exhibited a longer stability than those using the liquid-based electrolyte.

1. Graphene Nanosheets as Counter Electrodes for Dye-Sensitized Solar Cells

1.1. Introduction

Dye-sensitized solar cells (DSSCs) were first reported by Professor Grätzel in 1991. The advantages of DSSCs include high efficiency, low cost, simple structure, and easy fabrication. Therefore, DSSCs have attracted considerable attention in the academic community. A typical DSSC device structure includes a transparent conductive substrate, TiO_2 nanoparticle thin film, dye, electrolyte, and Pt counter electrode (CE). The role of a DSSC CE is to catalyze the reduction of the I_3^- ions in the electrolyte that is produced during the regeneration of oxidized dyes, which enables the dyes to return from an excited state to a ground state. Platinum (Pt) is typically used as a CE material because it yields highly efficient DSSCs. However, as a noble metal, Pt is relatively expensive, which is a considerable obstacle for the large-scale application of DSSCs. Therefore, a highly efficient replacement material for Pt is a crucial focus of DSSC-related studies.

Graphene possesses unique and exceptional material properties, such as high mechanical strength (approximately 1100 GPa), high thermal conductivity (approximately 5000 $Wm^{-1}K^{-1}$), and high carrier mobility (200,000 $cm^2V^{-1}s^{-1}$). Several research teams have also used graphene to fabricate DSSC CEs. This study used GNs to fabricate novel CEs, including GNs, GN-Pt composite, and GN-Pt stacked CEs for DSSCs. The electrode properties of the various CEs were analyzed using scanning electron microscopy (SEM), atomic force microscopy (AFM), Raman spectroscopy, X-ray photoelectron spectroscopy (XPS), energy dispersive X-ray spectrometry (EDS), and cyclic voltammetry (CV). The various GN CEs were investigated to identify the correlation between the CE fabrication conditions and DSSC characteristics and performance.

1.2. Experiments

Fabrication of the graphene nanosheets counter electrodes

Fig. 1 shows a schematic diagram of the DSSC structure with GN-Pt stacked CEs. The suspension of GNs was prepared as follows. First, 40 mg of ethyl cellulose was added to 2 g of α-terpineol and mixed thoroughly. Subsequently, 10 mg of GN powder (Enerage, graphene P-MF10) was added to the solution, and the solution was mixed using ultrasonic vibration for 30 min. The CEs were fabricated as follows. First, two small holes were predrilled into an FTO glass substrate to allow injection of electrolytes. Subsequently, the FTO substrate was ultrasonically cleaned with deionized water for 3 min, cleaned with alcohol for another 3 min, and then blow-dried with nitrogen gas. In this study, the GN CEs were fabricated using a spin-coating method (2000 rpm for 30 s) to produce a GN thin film on the FTO substrate. The electrodes were sintered at various temperatures (200, 300, 400, and 500 ºC) for 30 min in an air or nitrogen atmosphere. The GN-Pt composite CEs were fabricated by first adding the GN suspension to a Pt nanoparticle paste (Eversolar, Pt-200) at a 1:6 weight ratio and mixed thoroughly, and then coating the GN-Pt mixture onto the FTO substrate by using the doctor-blade method. Finally, the GN-Pt composite CEs were sintered at 400 ºC in a nitrogen atmosphere for 30 min. The GN-Pt stacked CEs were fabricated by first spin coating the GN suspension uniformly onto the FTO substrate at 2000 rpm for 30 s, and then sintering the samples at 400 ºC in a nitrogen atmosphere for 30 min to form the GN layer. The doctor-blade method was then used to coat the Pt paste onto the GN layer, and finally the GN-Pt stacked samples were sintered at 400 ºC in air for 30 min. Additionally, a reference Pt CE was

fabricated by coating the Pt paste onto the FTO substrate by using the doctor-blade method, and then sintering the coated samples at 400 ºC in air for 30 min.

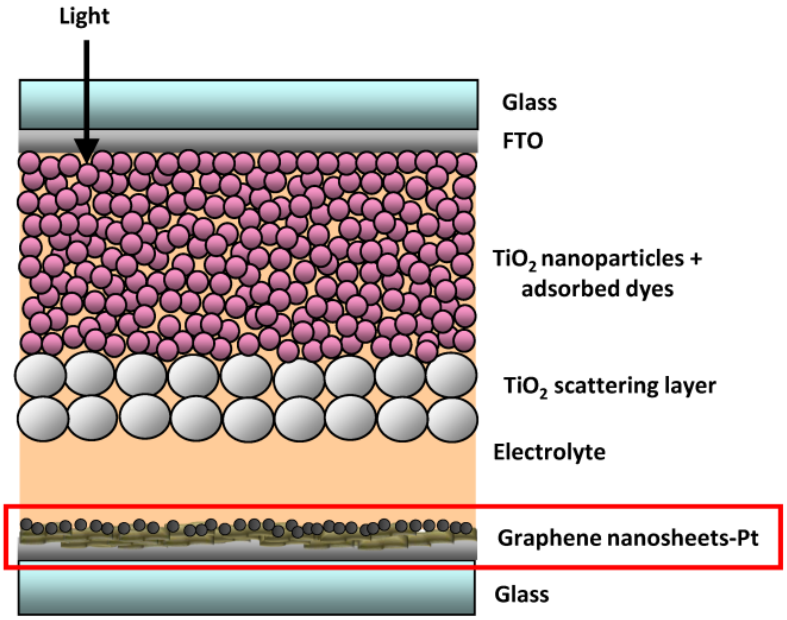

Fig. 1. The schematic diagram of the DSSC structure with GN-Pt stacked CEs.

Characterization of counter electrodes

In this study, the following analytic techniques were used to characterize the material properties of various CEs: scanning electron microscopy (SEM) was used to observe the sample surface morphologies; atomic force microscopy (AFM) was employed to measure the roughness and surface area of the sample; Raman spectroscopy was used to analyze the quality of the electrode; X-ray photoelectron spectroscopy (XPS) was used to inspect the quality and bonding conditions of the CEs; energy-dispersive X-ray spectroscopy (EDS) was adopted to observe the elemental ratios of the CEs; and cyclic voltammetry CV was used to measure the catalytic activities of the electrodes.

Dye-Sensitized Solar Cell Fabrication

The DSSC CEs were fabricated according to the process described in previous section. The DSSC working electrodes were fabricated by first cleaning the FTO conductive glass substrate and attaching scotch tape templates that were prepared by punching 4-mm-diameter holes in them (approximately 0.126 cm^2). The templates were used for the device coating area. A 20-nm TiO_2 paste was coated onto the FTO substrate by using the doctor-blade method. The samples were then heated at 150 ºC for 10 min. After cooling to room temperature, the coating procedure was repeated to obtain a TiO_2 working electrode with an approximate thickness of 12 μm. Subsequently, the same method was used to coat another scattering layer using 200-nm TiO_2 paste. Subsequently, the sample was sintered in a high-temperature furnace at 500 ºC for 30 min. After cooling to 80 ºC, the TiO_2 electrode was immersed in the prepared dye solution for 20 h. The dye solution used in this experiment was 0.5 mM N719 dye with 0.5 mM chenodeoxycholic acid added (CDCA) as a coabsorbent. The solvent comprised a 1:1 volumetric mixture of acetonitrile and tertbutyl alcohol. A 60-μm-thick sealing foil was cut to outer and inner (hollow) dimensions of 2.5×2.5 cm^2 and 0.8×0.8 cm^2, respectively. The sealing foil was employed to assemble the working electrode and counter electrode by using a hot press method at a temperature, pressure, and pressing time of 130 ºC,

3 kg/cm^2, and 3 min, respectively. After cooling the device to room temperature, a micropipette was used to inject approximately 5 μL of electrolyte into the DSSC devices. The electrolyte solutions comprised 0.6 M ionic liquid 1-butyl-3-methylimidazolium iodide (BMII), 0.05 M LiI, 0.03 M I_2, 0.5 M 4-tert-butyloyridine (4-TBP), 0.1 M guanidine thiocyanate (GuSCN), and a 5:1 mixture (by volume) of acetonitrile and valeronitrile. Subsequently, the 0.8×0.8 cm^2 trimmed sealing foils and glass plates were used to encapsulate the holes on the CEs at a temperature of 130 ºC and a pressure of 3 kg/cm^2 to prevent leakage and evaporation of the electrolyte. Finally, the solar cell surfaces were cleaned using ethanol.

DSSC Characterization

The current density-voltage (J-V) characteristics of the DSSCs were measured under illumination of the simulated AM1.5G solar light from a 550-W Xenon lamp solar simulator. The incident light intensity was calibrated to 100 mW/cm^2 by using a reference Si photodiode equipped with an infrared-cutoff filter (KG-5, Schott) to reduce the spectrum mismatch in the region of 350-750 nm between the simulated light and AM 1.5G to less than 2%. The reference cell was certificated by Bunkoh-Keiki Co Ltd, Japan. Photocurrent-voltage curves were obtained by applying an external bias voltage to the cell and measuring the generated photocurrent. The J-V characteristics of the DSSCs were used to extract the short-circuit current density (J_{SC}), open-circuit voltage (V_{OC}), fill factor (FF), and power conversion efficiency of the DSSCs. The incident monochromatic photon-to-current conversion efficiency (IPCE) spectra were measured using a 150-W Xenon arc lamp as the light source, which was coupled to a monochromator. The IPCE data were obtained by illuminating the solar cells monochromatic light at a wavelength sampling interval of 5 nm from 300 to 750 nm, and by measuring the short-circuit current of the solar cells. The IPCE measurement was performed under the full computer control.

Furthermore, electrochemical impedance spectroscopy (EIS) was performed to measure the cell impedance by using an impedance analyzer with a 0.1 Hz to 1 MHz frequency range. During the impedance measurement, the cell was under the constant AM 1.5G 100 mW/cm^2 illumination. The impedance of the cell (from 0.1 Hz to 1 MHz) was measured by applying a bias at the V_{OC} of the cell (i.e., under no dc electric current) and by using an AC amplitude of 10 mV.

1.3. Results and Discussion

Fig. 2 shows the SEM images of the various CEs. The Pt nanoparticles in Fig. 2(a) are distributed on the substrate with particle sizes ranging from approximately 5 to 10 nm. Fig. 2(b) shows the SEM image of the GN CEs fabricated in this study. The image shows that the GNs are extremely thin, resembling a partially folded and sheet-like structure; the dimensions of these GNs cover approximately 10 μm and are uniformly distributed on the substrate. The SEM image of the GN-Pt composite CEs in Fig. 2(c) shows spherical Pt nanoparticles and sheet-like GNs, with a portion of Pt nanoparticles trapped within the GNs. In addition, the GNs are partially agglomerated. The trapped Pt nanoparticles and agglomerated GNs may reduce the catalysis and conductivity of the CEs. Fig. 2(d) shows the SEM image of the GN-Pt stacked CEs. The image shows that a dense formation Pt nanoparticles adhering to the sheet-like GNs, yielding a high surface area CE.

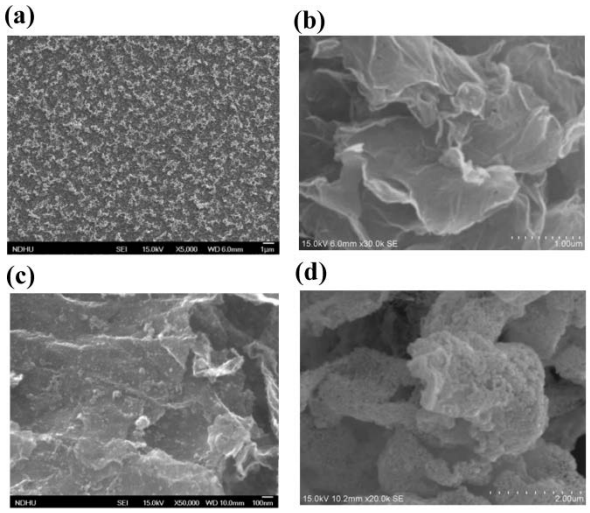

Fig. 2. The SEM images of various CEs.

Fig. 3 shows the AFM images of the various CEs. The AFM results show that the surface roughness of the Pt, GN, GN-Pt composite, and GN-Pt stacked CEs are 12.55 nm, 53.93 nm, 21.16 nm, and 61.70 nm, respectively. The surface area of the Pt (Fig. 3(a)), GN, GN-Pt composite, and GN-Pt stacked CEs are 18.24 μm^2, 51.32 μm^2, 21.46 μm^2, and 56.48 μm^2, respectively. The results indicate that the GN CEs (Fig. 3(b)) and GN-Pt stacked CEs (Fig. 3 (d)) provide large roughness and surface area. On the other hand, the GN-Pt composite CEs (Fig. 3(c)) exhibits lower surface roughness and surface area, which is due to the agglomeration of GNs.

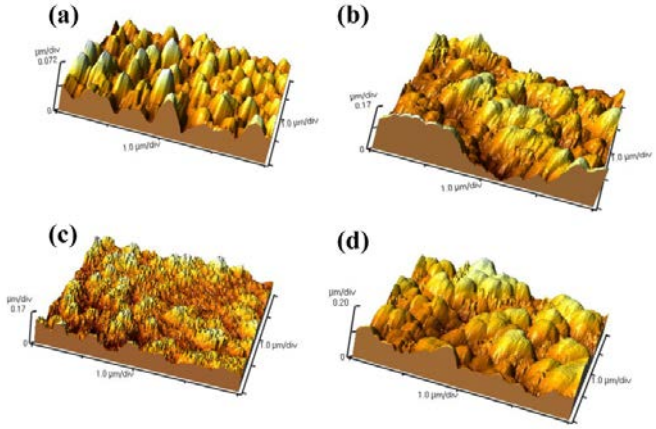

Fig. 3. The AFM images of various CEs.

Raman spectroscopy is an essential analysis technique for determining the sample quality of graphene. This technique involves using a laser to excite the sample and observing the photon-phonon interactions to determine the vibration and rotation modes of the lattices and molecules. In this study, a 532-nm laser beam was used as the excitation source. Fig. 4 shows the Raman spectra of the GN CEs sintered at 300 ºC, 400 ºC, and 500 ºC in air and nitrogen atmospheres. When sintered at 300 ºC, the fluorescence effect is severe, causing interference with the measurement of the peak values. This occurs because the sintering temperature of 300 ºC is insufficient to trigger the evaporation or combustion of the organic substances, such as the solvent or adhesives in the CEs. When sintered at 400 ºC (in air and in nitrogen atmospheres) and 500 ºC (in nitrogen atmosphere), three peaks in Raman spectra can be observed at 1350, 1580, and 2700 cm^{-1}, respectively, representing the D, G, and 2D bands.

Previous studies have indicated that decreasing the number of graphene layers yielded 2D-band wavenumbers approaching 2700 cm^{-1}. The Raman results demonstrate that the sintering process produces graphene nanosheets CEs. In addition, the Raman peak values are not clearly distinguishable after sintering at 500 ºC in air (Fig. 4(a)). This occurs because the GNs are dissipated and volatilized when sintering at excessively high temperatures in air.

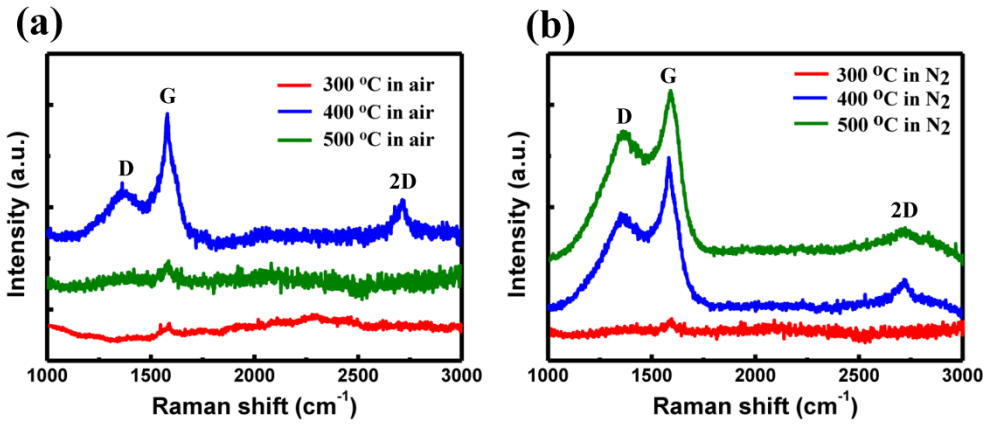

Fig. 4. The Raman spectra of the GN CEs sintered at 300, 400, and 500 ºC (a) in air and (b) in nitrogen atmospheres.

XPS was used to examine the quality and bond type of the GN CEs. Graphene consists of a honeycomb structure comprising C-C sp^2 orbital. When defects and impurities exist, the C-C bonds change into functional groups exhibiting various bond types, including C-OH, C-O-C, O-C=O, C=O, and C=OOH. The binding energies measured for C-C sp^2, C-OH, C=O, and C=OOH are 284.6, 286.7, 288.0, and 289.1 eV, respectively. Fig. 5(a) shows the XPS results of the GN CEs sintered at 200, 300, 400, and 500 ºC in an air atmosphere. The results indicate that the GN CEs sintered at 200 ºC yield higher peak values, indicating defective bonds. When the sintering temperature is increased to 300 ºC, substantially fewer defect-causing functional groups were observed. At sintering temperatures of 400 ºC and 500 ºC, the defects almost completely disappear. Furthermore, when sintered at 500 ºC, the intensity of the C-C peak decrease, which occurs because of the dissipation and volatilization of the graphene. Fig. 5(b) shows the XPS results of the GN CEs sintered at various temperatures in a nitrogen atmosphere. The results show that sintering in a nitrogen atmosphere prevents the dissipation and volatilization of the graphene. Therefore, the intensity of the C-C peak of the sample sintered at 500 ºC in nitrogen is stronger than that of sintered in air. The results show that the sample sintered at 400 ºC in a nitrogen atmosphere yields the optimal graphene quality.

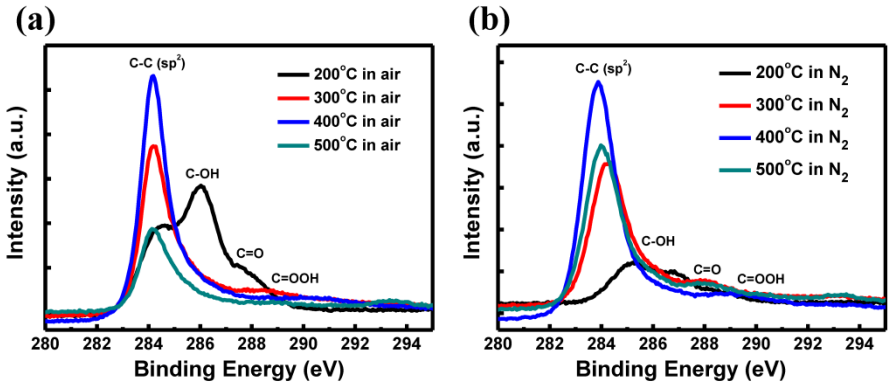

Fig. 5. The XPS results of the GN CEs sintered at various temperatures.

EDS was employed to analyze the element types and contents of the CEs. Fig. 6 shows the EDS results of the GN CEs and GN-Pt stacked CEs. The elemental composition of the GN CEs is 100 % carbon, whereas that of the GN-Pt stacked CEs is C and Pt, with the C-Pt weight ratio of 9.05 to 90.95 (equivalent to an atomic ratio of 61.78:38.22), respectively.

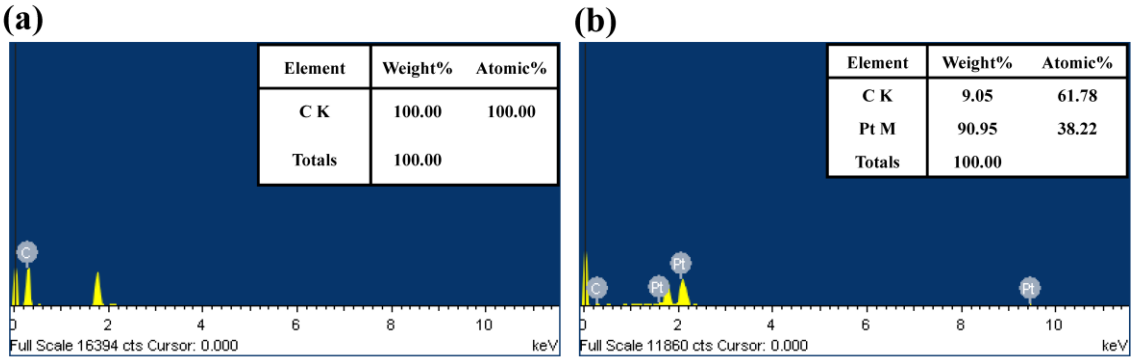

Fig. 6. The EDS results of the GN CEs and GN-Pt stacked CEs.

In this study, CV was used to analyze the electrochemical catalytic properties of the various CEs. The CV results in Fig. 7 reveal the oxidation reaction of $3I^- \rightarrow I_3^- + 2e^-$ at 0.6-0.8 V and the reduction reaction of $I_3^- + 2e^- \rightarrow 3I^-$ at 0.2-0.4 V. The magnitude of the reduction peaks can be used to determine the electrochemical catalytic activities of the various CEs. The experimental results indicate that the catalytic activities of the various CEs are ranked in descending order as follows: GN-Pt stacked, GN-Pt composite, Pt, and GN CEs; the reduction current densities (I_{ph}) are 1.43, 1.12, 0.74, and 0.51 mA/cm^2, respectively. The CV results show that the GN-Pt stacked CE structure yields the optimal catalytic activity.

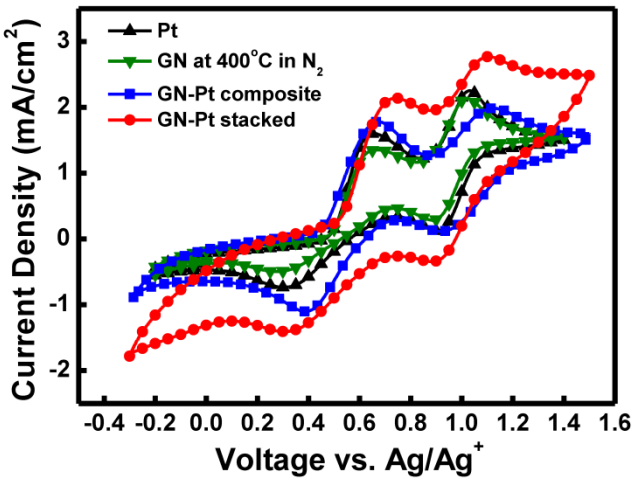

Fig. 7. The CV results of various counter electrodes.

In this study, GN CEs were fabricated in various gas atmospheres and at various temperatures. Fig. 8(a) shows the J-V curves of the DSSCs using the GN CEs sintered in air at 200, 300, 400, and 500 ºC, respectively. Table 1 shows a summary of the J-V measurement parameters. The results indicate that the GN CEs sintered at 400 ºC in air yield the optimal device efficiency; the corresponding Jsc, Voc, FF, and efficiency are 13.86 mA/cm^2, 0.56 V, 0.19, and 1.47 %, respectively. The DSSCs with the GN CEs sintered at 400 ºC in air exhibit satisfactory Jsc; however an inadequate FF results in low device efficiency. The experimental results indicate that a portion of GNs sintered in air transforms into graphene oxide, thus decreasing the material conductivity. Therefore, this study used nitrogen sintering to prevent

graphene oxidation. Fig. 8(b) shows the J-V curves of the DSSCs based on the GN CEs sintered in nitrogen at 200, 300, 400, and 500 ºC. The results indicate that the GN CEs sintered in a nitrogen atmosphere exhibits superior FF and device efficiency compared with those sintered in air. Furthermore, sintering at a temperature of 400 ºC yields the optimal efficiency of 5.09 % (Jsc=14.76 mA/cm^2, Voc=0.74 V, FF=0.47). These results are attributed to the sintering of GN CEs under a nitrogen atmosphere, which effectively reduces the graphene oxidation and prevents CO_2 production resulting from oxidation from the surrounding atmosphere. Moreover, sintering GN CEs in a nitrogen atmosphere reduces the dissipation and volatilization of the GNs. Furthermore, this study fabricated GN-Pt composite and GN-Pt stacked CEs to investigate the influence of various CE structures on DSSC device efficiency. These two CEs were sintered at 400 ºC in a nitrogen atmosphere for 30 min. Fig. 8(c) shows the J-V curves and Table 1 shows the respective measured values of the various CEs. The power conversion efficiency of the DSSCs based on Pt CEs, GN-Pt composite, and GN-Pt stacked CEs are 7.32 % (Jsc=15.01 mA/cm^2, Voc=0.70 V, and FF=0.69), 6.35 % (Jsc=16.73 mA/cm^2, Voc=0.73 V, FF=0.52), and 8.54 % (Jsc=18.26 mA/cm^2, Voc=0.72 V, FF=0.65), respectively. The results indicate that incorporating GNs into CEs improves the Jsc values. However, the DSSCs with the GN-Pt composite CEs exhibit a decreased FF and device efficiency. The low FF and efficiency of DSSCs based on the GN-Pt composite CEs is the result of the agglomeration of the GNs and low conductivity of the GN-Pt composite CEs.

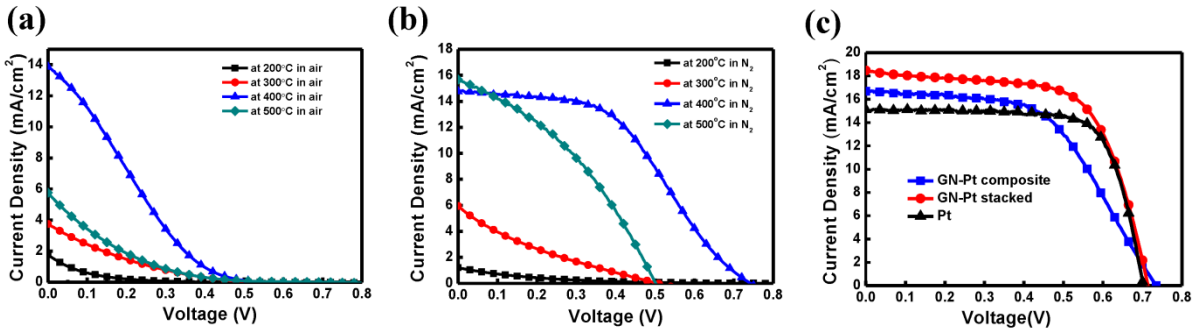

Fig. 8(a). The J-V curves of the DSSCs based on various GN CEs.

Table 1. The device parameters obtained from the J–V curves.

Counter electrode	Jsc (mA/cm^2)	Voc (V)	Fill Factor	Efficiency (%)
GN (200 °C in air)	1.77	0.60	0.06	0.06
GN (300 °C in air)	3.74	0.50	0.16	0.30
GN (400 °C in air)	13.86	0.56	0.19	1.47
GN (500 °C in air)	5.76	0.73	0.09	0.39
GN (200 °C in N_2)	1.21	0.78	0.11	0.09
GN (300 °C in N_2)	5.96	0.66	0.14	0.54
GN(400 °C in N_2)	14.76	0.74	0.47	5.09
GN (500 °C in N_2)	15.67	0.50	0.37	2.91
Pt	15.01	0.70	0.69	7.32
GN-Pt composite	16.73	0.73	0.52	6.35
GN-Pt stacked	18.26	0.72	0.65	8.54

Figs. 9(a) and 9(b) show the IPCE results of the DSSCs based on the GN CEs sintered at 200, 300, 400, and 500 ºC in air and nitrogen atmospheres. A sintering temperature of 400 ºC yields the optimal IPCE values in the air-sintered GN CEs, whereas a temperature of 500 ºC yields the optimal IPCE values in the nitrogen-sintered GN CEs. The IPCE results are

consistent with the Jsc values of the J-V measurements. Fig. 9 (c) shows that the IPCE values of the Pt, GN-Pt composite, and GN-Pt stacked CEs are ranked in descending order as follows: GN-Pt stacked, GN-Pt composite, and Pt CEs. The IPCE results are consistent with the Jsc values of the J-V measurements.

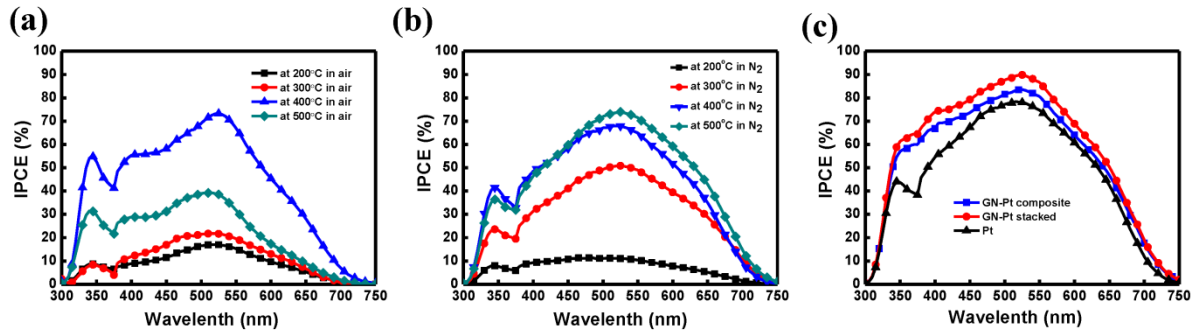

Fig. 9. The IPCE results of the DSSCs based on various CEs.

Figs. 10(a) and 10(b) show the EIS Nyquist plots of the DSSCs based on the GN CEs sintered at 200, 300, 400, and 500 ºC in air and nitrogen atmospheres, respectively. The Nyquist plots of the DSSCs typically consist of three distinct semicircles. In the figures, the semicircle corresponding to the charge-transfer processes at the CE-electrolyte interface is overridden by the semicircle corresponding to the charge-transfer processes at the TiO_2-dye-electrolyte interface. The DSSC EIS results show that among the various sintering temperatures in air, the CEs sintered at 400 ºC yielded the lowest impedance (approximately 510 Ω) at the TiO_2-dye-electrolyte interface. The DSSCs based on the CEs sintered in nitrogen exhibit markedly smaller impedance values. The DSSC EIS resistance of the GN CEs sintered in nitrogen at 400 and 500 ºC are 275 and 315 Ω, respectively. The experimental results indicate that the nitrogen-sintered GN CEs exhibit superior conductive properties and catalytic activities compared with those of the air-sintered GN CEs. Fig. 10 (c) shows the EIS Nyquist plots of the DSSCs based on the Pt, GN-Pt composite, and GN-Pt stacked CEs. The results show that the DSSCs based on GN-Pt stacked CEs exhibit the smallest semicircle at the CE-electrolyte interface. The optimal impedance characteristics of the GN-Pt stacked CEs are attributed to the large surface area of the GNs between the FTO and Pt layers providing additional surface area for the Pt nanoparticles to adhere to, which enables the GNs with high conductivity to augment the electron transfer properties in GN-Pt stacked CEs. On the other hand, the DSSCs based on the GN-Pt composite CEs exhibit the largest impedance at the CE-electrolyte interface. The high impedance of the GN-Pt composite CEs is attributed to the agglomeration of GNs and the Pt nanoparticles trapped in the GNs reducing the conductivity.

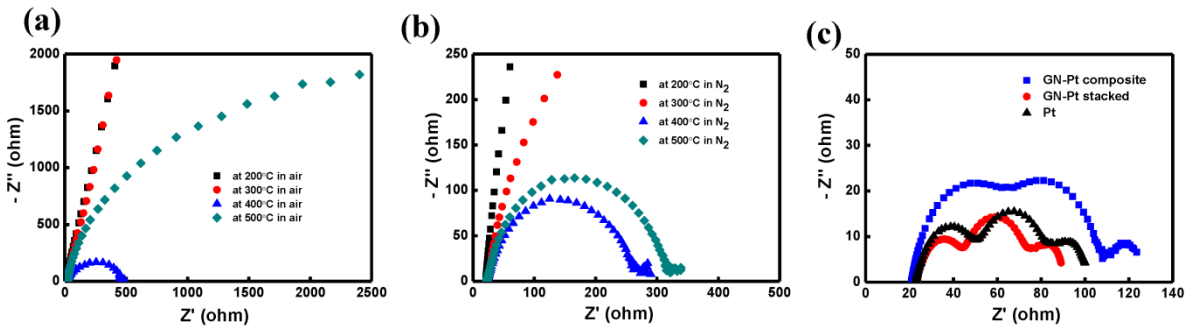

Fig. 10. The EIS Nyquist plots of the DSSCs based on various CEs.

1.4. Conclusions

This study comprised two parts. In the first part, the application of GN CEs in DSSCs and the influences of various sintering conditions of CEs on DSSC efficiency were investigated. In the second part, the influences of GN-Pt composite and GN-Pt stacked CEs on the efficiency of DSSCs were studied. The CE properties were characterized by SEM, AFM, Raman spectroscopy, XPS, EDS, and CV, and the characteristics of the DSSCs based on the various CEs were analyzed using J-V, IPCE, and EIS measurements. First, various temperatures and gas atmospheres were applied to sinter the GN CEs to determine the optimal sintering conditions. The results indicated that sintering at 400 ºC for 30 min in a nitrogen atmosphere yielded the optimal electrode quality and DSSC efficiency. In addition, the GN CEs sintered at temperatures higher than 400 ºC in air exhibited severe dissipation and volatilization of the GNs. Next, this study investigated two novel GN-based CEs for DSSCs. The results show that the DSSCs based on conventional Pt CEs yielded an efficiency of 7.32 %, those based on the GN-Pt composite CEs yielded a device efficiency of 6.35 %, and those based on the GN-Pt stacked CEs yielded an optimal efficiency of 8.54 %, indicating a 16.7 % improvement compared with the DSSCs based on conventional Pt CEs.

2. Enhancing the efficiency of gel-state dye-sensitized solar cells

2.1. Introduction

Structurally, DSSC devices comprise a transparent conductive substrate, nanoporous titanium dioxide (TiO_2) semiconductor thin films, dyes, electrolytes, and a platinum (Pt) counter electrode. Featuring redox properties, electrolytes serve as a key component in DSSC devices; they provide dyes with electrons to enable the dyes to return from an excited state to the ground state, thereby completing dye regeneration. Conventional DSSC electrolytes are mostly liquid-based. However, solvent evaporation and leakage tend to occur with liquid-based electrolyte, which shortens the stability of DSSC devices. Therefore, in recent years, numerous research teams have studied and improved DSSC electrolytes to enhance device stability. According to a recent literature review, the main research directions are currently focused on replacing conventional liquid-based electrolytes with ionic liquid, gel, or solid-based electrolytes. Previous studies have indicated that gel-based electrolytes can be obtained by adding polymethylmethacrylate (PMMA) to liquid-based electrolytes. PMMA is a long-chain polymer compound with properties such as high material softness, high mechanical strength, low crystallization tendencies, and high material transmittance; thus, it is an excellent gelator for preparing gel-based electrolytes. Adding PMMA to electrolytes causes electrolyte gelling, thereby reducing electrolyte evaporation and leakage. However, adding gelators to electrolytes decreases the conductivity of the electrolytes and increases the impedance of the electrolyte layer, thereby lowering the power conversion efficiency of DSSCs. This study focused on fabricating gel-based electrolytes by mixing PMMA with a liquid-based electrolyte to reduce electrolyte evaporation and leakage, thus extending the life of DSSC devices. By adding lithium bis(trifluoromethanesulphonyl)imide (LiTFSI) and camphorsulfonic acid ($C_{10}H_{16}O_4S$) to gel-based electrolytes, the current study successfully enhanced the conductivity of gel-based electrolytes, further increasing the power conversion efficiency of gel-based DSSCs.

2.2. Experimental Methods

Preparation of Gel-Based Electrolytes

First, a gelator and a liquid-based electrolyte solution were prepared. The gelator was prepared by mixing PMMA and propylene carbonate at a ratio of 1 to 2 (i.e., 0.5 g of PMMA to 1 mL of propylene carbonate), stirring the mixture for 3 hr at 90 ºC, and cooling the

mixture at 4 ºC in a refrigerator for 24 hr to remove bubbles from the solution. The liquid-based electrolyte solution contained 0.6 mol/L (M) BMII, 0.05 M LiI, 0.03 M I_2, 0.5 M 4-tert-butyloyridine, 0.1 M guanidine thiocyanate, and acetonitrile and valeronitrile at a volume ratio of 5:1.

Fig 11(a) shows the device structure of a gel-state dye-sensitized solar cell. This study examined the effect of mixing gelator and liquid-based electrolyte solution of varying volume ratios on the properties of fabricated devices. Gel-based electrolytes were obtained by mixing the gelator and liquid-based electrolyte solution at the ratios of 1:0.5, 1:1, and 1:1.5. The properties of the electrolytes and devices were then analyzed. In addition, the effect of adding LiTFSI (Fig.11(b)) and $C_{10}H_{16}O_4S$ (Fig. 11(c))to the gel-based electrolytes on the device properties was examined. Specifically, 0.1 M LiTFSI and 0.1 M $C_{10}H_{16}O_4S$ were separately added to the gel-based electrolytes to analyze the electrolyte and device properties.

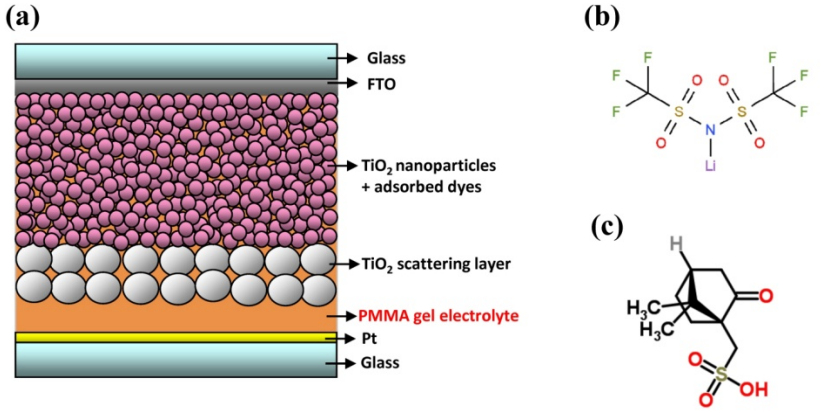

Fig. 11. (a) Device structure of a gel-state dye-sensitized solar cell. Molecular structures of (b) LiTFSI and (c) $C_{10}H_{16}O_4S$.

Fabrication of DSSC Devices

The DSSC working electrode was fabricated as follows. First, a piece of fluorine doped tin oxide (FTO) conductive glass was cleaned. Subsequently, strips of 3M tape with 3-mm-diameter holes punched into them were fixed to the glass. The holes, which had an area of approximately 0.126 mm^2, served as the coating area of the devices. A 25-nm layer of TiO_2 paste was coated uniformly onto the specimen by using the doctor blade printing method. The coated specimen was heated for 10 min at 150 ºC and allowed to cool to room temperature. The TiO_2 coating procedure was repeated, from which an approximately 12-µm-thick working electrode was obtained. Another layer of TiO_2 paste composed of approximately 200-nm particles was subsequently coated using the same method to serve as the scattering layer. The specimen was then placed inside a furnace and sintered at 500 ºC for 30 min. After the TiO_2 electrode was cooled to 80 ºC, it was soaked in prepared dyes for 24 hr and then removed from the dye. Regarding the dye preparation, 0.5 mM N719 dye was mixed with 0.5 mM chenodeoxycholic acid, with the latter material serving as a coabsorbent in this experiment. Moreover, the solvent was prepared by mixing a 1:1 volume ration of acetonitrile and tert-Butyl alcohol.

The method for fabricating the DSSC counter electrode is described as follows. A piece of FTO conductive glass with two predrilled holes (for pouring the electrolyte solution) was used as the substrate. The specimen was then washed with deionized water and alcohol for 3 min by using an ultrasonic cleaner. The specimen surface was then dried using nitrogen gas. A Pt nanoparticle paste was uniformly applied onto the FTO substrate by using the doctor-blade printing method. The specimen was placed inside a furnace and sintered at 450 ºC for 30 min. The Pt counter electrode was fabricated when the specimen cooled naturally to the room temperature. The method for encapsulating the DSSC devices is presented as follows: A piece

of 60-μm-thick sealing foil was cut into a 2.5×2.5 cm^2 with a 0.8×0.8 cm^2 area cut from the center. The sealing foil was used to assemble the working and counter electrodes. The assembled device was continually pressurized at 3 kg/cm^2 at 130 ºC for 3 min to facilitate adhering the upper and lower electrodes. After cooling, the assembled device was injected with approximately 5 μL of gel-based electrolyte by using a trace dropper, and then heated at 60 ºC for 20 min to solidify the gel-based electrolyte. The preparation method of the gel-based electrolyte is described in previous section. Subsequently, the precut foil squares and glass substrate were used to seal the holes on the counter electrode at a pressure of 3 kg/cm^2 and at 130 ºC to prevent electrolyte evaporation and leakage. Finally, after the surface of the solar panel was cleaned using alcohol, fabrication of the DSSC device was completed.

2.3. Results and Discussion

Effect of Different Gelator to Liquid-Based Electrolyte Ratios on DSSC Device Properties

Four DSSC devices with different gelator to liquid-based electrolyte volume ratios: (i.e., 1:0.5, 1:1, 1:1.5, and 0:1(liquid electrolyte)) were fabricated and compared. The current density–voltage (J–V) curves of the devices were subsequently obtained, as shown in Fig. 12. The figure shows the short-circuit current density (Jsc), open-circuit voltage (Voc), fill factor, and efficiency (Eff.) of the devices. Table 2 show the device parameters obtained from the J–V curves. According to Fig. 12 and Table 2, the DSSC devices with electrolyte ratios of 1:0.5, 1:1, 1:1.5, and 0:1 respectively obtained a Jsc of 12.65, 15.57, 15.86, and 16.16 mA/cm^2; a Voc of 0.67, 0.67, 0.69, and 0.68 V; and a fill factor of 0.65, 0.65, 0.61, and 0.64. The power conversion efficiency of the devices revealed that electrolyte with an electrolyte ratio of 0:1 achieved the optimal result (7.04%), followed that with an electrolyte ratio of 1:1 (6.75%), 2:3 (6.62%), and 2:1 (5.51%). The results indicated that among the four gel-based electrolytes, the 1:1 electrolyte ratio exhibited the most advantageous device efficiency. However, the DSSC devices with the gel-based electrolytes achieved lower efficiency compared with DSSC devices that used a liquid-based electrolyte.

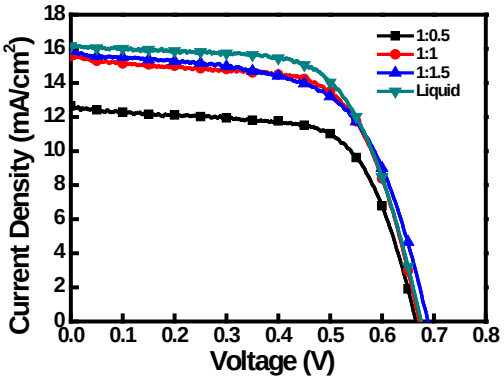

Fig. 12. The current density–voltage (J–V) curves of the devices.

Table 2. The device parameters obtained from the J–V curves.

Electrolyte	Jsc (mA/cm^2)	Voc (V)	Fill Factor	Efficiency (%)
1:0.5	**12.65**	**0.67**	**0.65**	**5.51**
1:1	**15.57**	**0.67**	**0.65**	**6.75**
1:1.5	**15.86**	**0.69**	**0.61**	**6.62**
Liquid	**16.16**	**0.68**	**0.64**	**7.04**

This study also conducted an incident photo-to-current conversion efficiency (IPCE) test on the various DSSC devices. Fig. 13 shows the IPCE results of the devices. Because the N719 dye was used in all of the DSSC devices, the main absorbance range of all the devices was 400–650 nm. Specifically, peaks near 350 nm indicated the peak absorption value of TiO_2 films, whereas those near 530 nm represented the peak absorption value of the N719 dye. The IPCE experiment result showed that the device with the 0:1 liquid-based electrolyte exhibited the highest IPCE peak value (77 %), those with the 1:1 and 1:1.5 gel-based electrolytes obtained similar IPCE peak values (approximately 70 %), and that containing the 1:0.5 gel-based electrolyte attained the lowest IPCE value (64 %). The Jsc values of the devices with the various electrolytes were determined according to the J–V curves; the devices with the 1:0.5, 1:1, and 1:1.5 gel-based electrolytes and the device with the 0:1 liquid-based electrolyte respectively obtained Jsc values of 12.65, 15.57, 15.86, and 16.16 mA/cm^2. The results revealed that the trends of the IPCE peaks and Jsc values were identical.

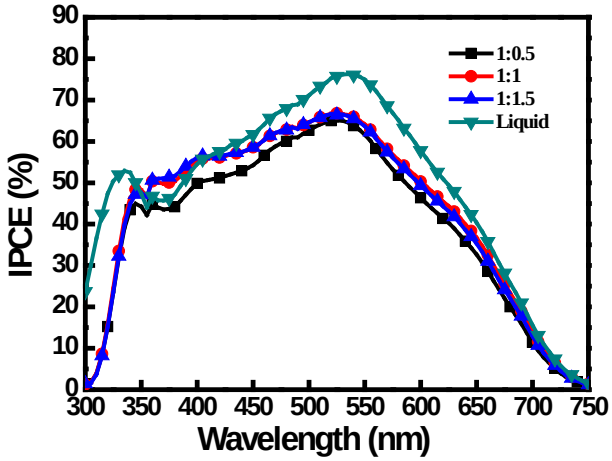

Fig. 13. The IPCE results of the devices.

Subsequently, the DSSC devices were analyzed through electrochemical impedance spectroscopy (EIS). The results are presented in Fig. 14. The EIS Nyquist plot contains three semicircles, representing the impedance of various interfaces in the DSSC devices. The semicircle on the left shows the impedance of the counter electrode/electrolyte interface, the semicircle in the middle presents the impedance of the TiO_2/dye/electrolyte interface, and the semicircle on the right shows the impedance of the electrolytes. The results showed that regarding the counter electrode/electrolyte interface, the devices with an electrolyte ratio of 1:1 or 1:1.5 exhibited relatively low impedance values. Concerning the TiO_2/dye/electrolyte interface, the device with the liquid-based electrolyte also demonstrated low impedance values, in which the impedance value, listed in ascending order, was device with an electrolyte ratio of 1:1, 1:1.5, and 1:0.5. Because the TiO_2/dye/electrolyte interfacial impedance was mainly influenced by the number of photo-generated electrons, the lower TiO_2/dye/electrolyte interfacial impedance levels indicated a greater number of the photo-generated electrons. Furthermore, the impedance of the electrolyte solutions indicated the internal impedance of the electrolytes. The results revealed that the electrolyte ratio of 1:1 attained the lowest impedance value, followed by the electrolyte ratios of 1:1.5 and 1:0.5. Electrochemical impedance frequency analysis revealed that except for the liquid-based electrolyte, the 1:1 gel-based electrolyte demonstrated the optimal electrochemical properties. This measurement result accords with that of the J–V curve figure.

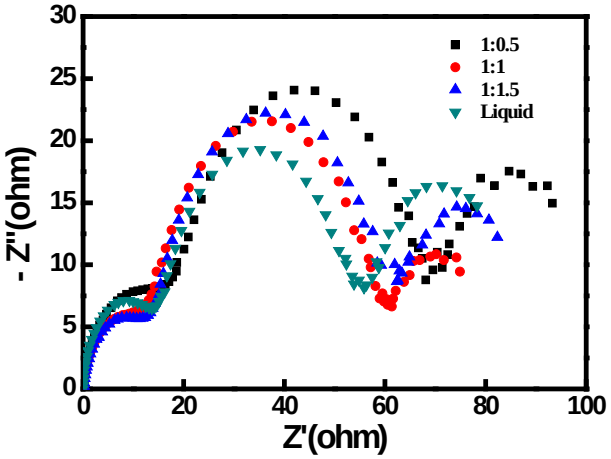

Fig. 14. The EIS Nyquist plots of various DSSC devices.

Enhancing the Efficiency of DSSC Devices by Adding LiTFSI and $C_{10}H_{16}O_4S$ to Gel-Based Electrolytes

The results in the previous section show that the DSSC device fabricated with a gelator to electrolyte solution volume ratio of 1:1 exhibited the optimal properties. Therefore, in the second part of this study, the 1:1 electrolyte was adopted as the control substance. The 0.1 M LiTFSI and 0.1 M $C_{10}H_{16}O_4S$ were separately added to the 1:1 gel-based electrolyte to analyze their effect on the electrolyte and device properties. First, a simple symmetric device was fabricated with two identical Pt electrodes, which were sealed with hot-melt sealing foils, and the gel-based electrolyte was injected between the electrodes. An electrochemical analyzer was employed to measure the electrochemical impedance spectrum of this device.

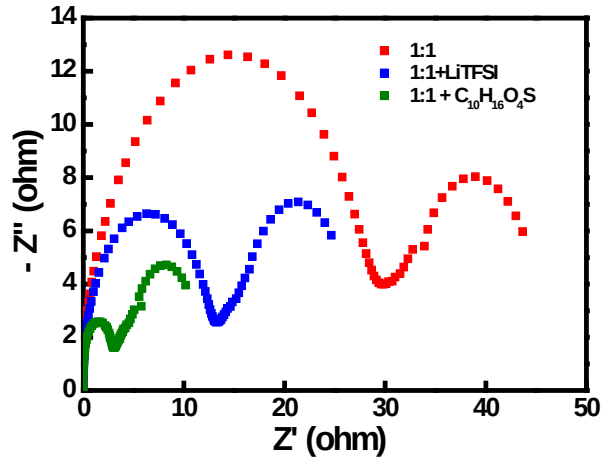

Fig. 15. The EIS results of various simple symmetric devices.

Fig. 15 shows the EIS results of various simple symmetric devices. The figure shows that when LiTFSI was added to the gel-based electrolyte, both the impedance values at the counter electrode/electrolyte interface and within the electrolyte decreased significantly. Moreover, the impedance value was further lowered when $C_{10}H_{16}O_4S$ was added to the gel-based electrolyte. The electrochemical impedance spectrum indicated that adding LiTFSI and $C_{10}H_{16}O_4S$ to the gel-based electrolytes effectively enhanced their conductivity. This study also used a conductivity meter (CON 500) to directly measure the conductivity of the electrolytes. Experimental data showed that the conductivity of the 1:1 gel-based electrolyte was 9.1 mS, that of the gel-based electrolyte with LiTFSI was 10.25 mS, and that of the

gel-based electrolyte with $C_{10}H_{16}O_4S$ was 10.12 mS, indicating that adding LiTFSI and $C_{10}H_{16}O_4S$ effectively enhanced the conductivity of gel-based electrolytes. This was attributed to the lithium (Li) ions in the LiTFSI being mobile in the noncrystalline area of the polymers, thus achieving ion transport and enabling the LiTFSI to attain favorable conductivity in polymers. The PMMA polymer in the gel-based electrolytes was a noncrystalline polymer. Its C=O bonds dissociated a considerable amount of LiTFSI, thus forming coordination bonds between the polymer and cation (Li^+). The flexible chain of the polymer was then used to surround the anions to limit anionic migration, thereby enhancing the migration rate of Li^+ ions and the ion mobility. Furthermore, the dissociation energy and low viscosity of the ions of the solvent were utilized to enhance the conductivity of the electrolyte. In addition, the reason why $C_{10}H_{16}O_4S$ increased the conductivity was inferred as follows: the C=O bonds of PMMA dissociated numerous hydrogen (H) ions from $C_{10}H_{16}O_4S$, thus forming coordination bonds between the polymer and cation (H^+). Moreover, $C_{10}H_{16}O_4S$ also contained C=O bonds, which dissociated H ions from PMMA to form coordination bonds. The flexible chain of the polymer was used to surround the anions to limit anionic migration, thereby enhancing both the migration rate of Hi^+ ions and the ion mobility. The production of a high number of H ions attracted more electrons, thereby enhancing the conductivity of the electrolyte.

Four DSSC devices with different electrolytes were fabricated and their properties were analyzed. The electrolytes were a liquid-based electrolyte, a 1:1 gel-based electrolyte, a 1:1 + LiTFSI gel-based electrolyte, and a 1:1 + $C_{10}H_{16}O_4S$ gel-based electrolyte. Fig. 16 shows the J–V curves of the DSSC with the different electrolytes. Table 3 presents the Jsc, Voc, fill factor, and Eff. of the devices. The results show that the DSSC devices with the liquid-based, 1:1 gel-based, 1:1 + LiTFSI gel-based, and 1:1 + $C_{10}H_{16}O_4S$ gel-based electrolytes respectively obtained Jsc values of 16.16, 15.57, 16.59, and 16.31 mA/cm^2; Voc values of 0.68, 0.67, 0.68, and 0.64 V; and fill factor values of 0.64, 0.65, 0.65, and 0.68. Regarding power conversion efficiency, the device with the 1:1 + LiTFSI gel-based electrolyte achieved the optimal effect (7.28 %), followed by those with the 1:1 + $C_{10}H_{16}O_4S$ gel-based electrolyte (7.11 %), liquid-based electrolyte (7.04 %), and 1:1 gel-based electrolyte (6.75 %). These results indicated that the DSSC device with the 1:1 + LiTFSI gel-based electrolyte possessed the highest power conversion efficiency. Moreover, the device with 1:1 + $C_{10}H_{16}O_4S$ gel-based electrolyte also achieved superior device efficiency compared with the device with liquid-based electrolyte.

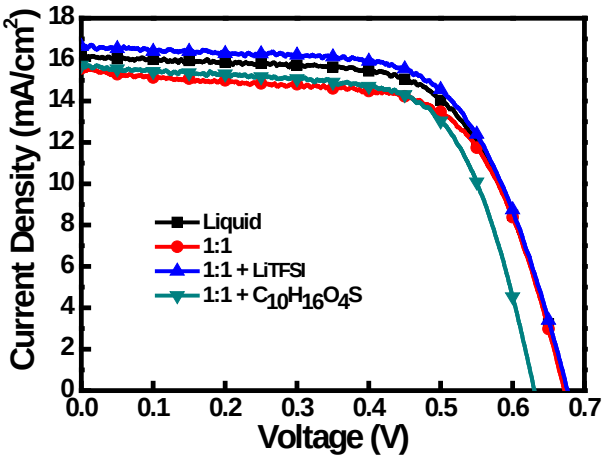

Fig. 16. The J–V curves of the DSSC with the different electrolytes.

Table 3. The device parameters obtained from the J–V curves.

Electrolyte	Jsc (mA/cm^2)	Voc (V)	Fill Factor	Efficiency (%)
Liquid	**16.16**	**0.68**	**0.64**	**7.04**
1:1	**15.57**	**0.67**	**0.65**	**6.75**
1:1 + LiTFSI	**16.59**	**0.68**	**0.65**	**7.28**
1:1 + $C_{10}H_{16}O_4S$	**16.31**	**0.64**	**0.68**	**7.11**

An IPCE analysis was conducted on the DSSC devices with the liquid-based, 1:1 gel-based, 1:1 + LiTFSI gel-based, and 1:1 + $C_{10}H_{16}O_4S$ gel-based electrolytes, the results of which are shown in Fig. 17. Because the N719 dye was used in all the DSSC devices, the main absorbance range was 400–650 nm for all devices. Specifically, peaks near 350 nm indicated the peak absorption value of TiO_2 films, whereas those near 530 nm represented the peak absorption value of the N719 dye. The IPCE experiment result indicated that the device with the 1:1 + LiTFSI gel-based electrolyte obtained the highest IPCE value (82%). The devices with the liquid-based electrolyte and 1:1 + $C_{10}H_{16}O_4S$ gel-based electrolyte achieved similar IPCE values (approximately 77 %). The device with the 1:1 gel-based electrolyte exhibited the lowest IPCE value (approximately 70 %). The Jsc values of the devices were determined using the J–V curves: the devices with the 1:1 + LiTFSI gel-based, liquid-based, 1:1 + $C_{10}H_{16}O_4S$ gel-based, and 1:1 gel-based electrolytes respectively attained Jsc values of 16.59, 16.16, 16.31, and 15.57 mA/cm^2. The results revealed identical trends in the IPCE peaks and Jsc values.

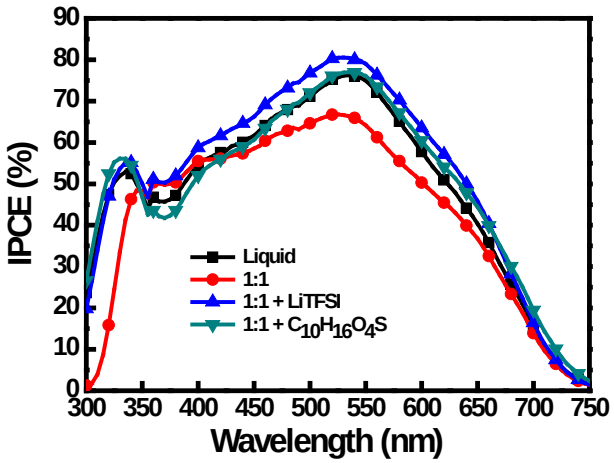

Fig. 17. The IPCE results of devices with the liquid-based, 1:1 gel-based, 1:1 + LiTFSI gel-based, and 1:1 + $C_{10}H_{16}O_4S$ gel-based electrolytes.

Subsequently, the various DSSC devices were analyzed through EIS. Fig. 18 shows the results. Regarding the counter electrode/electrolyte interface, the devices with the 1:1 + LiTFSI and 1:1 + $C_{10}H_{16}O_4S$ gel-based electrolytes attained slightly higher impedance values compared with the device with the liquid-based electrolyte. The cause for this phenomenon was attributed to the slightly higher interfacial conductivity between the counter electrode and gel-based electrolytes (containing PMMA) compared with that between the counter electrode and liquid-based electrolyte. Regarding the impedance of the TiO_2/dye/electrolyte interface, the gel-based electrolyte with LiTFSI attained the lowest impedance value, followed by the

gel-based electrolyte with $C_{10}H_{16}O_4S$, the liquid-based electrolyte, and the gel-based electrolyte alone. In addition, the results show that the 1:1 + $C_{10}H_{16}O_4S$ gel-based electrolyte attained the lowest impedance value, followed by the 1:1 gel-based electrolyte, and the 1:1 + LiTFSI gel-based electrolyte. This was attributed to the reduction in the viscosity of the gel-based electrolytes from the addition of LiTFSI, which caused bubbles to generate, thereby increasing the internal impedance of the electrolytes. These results accorded with those obtained from the impedance spectrum analysis of simple-model devices: liquid-based electrolytes possess relatively high impedance because of their tendency to generate bubbles. The EIS analysis results indicated that the device with the 1:1 + LiTFSI gel-based electrolyte exhibited the most advantageous properties, as indicated by the J–V curve.

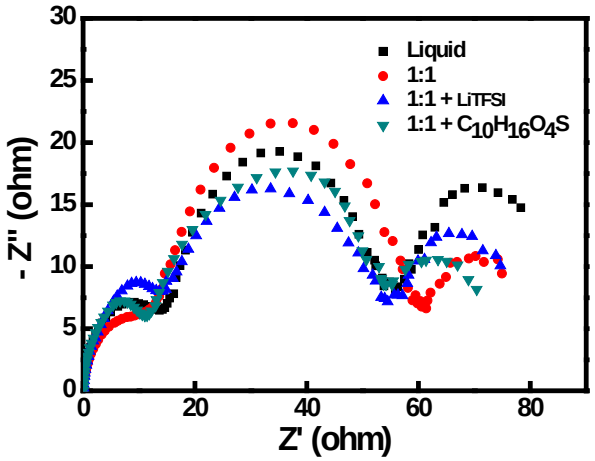

Fig. 18. The EIS results of devices with the liquid-based, 1:1 gel-based, 1:1 + LiTFSI gel-based, and 1:1 + $C_{10}H_{16}O_4S$ gel-based electrolytes.

This study also compared the stability of the DSSC devices with the gel-based and liquid-based electrolytes. Fig. 19 shows that after 1200 hours, the devices with the gel-based electrolytes retained 70~80% of their efficiency compared with the original devices. By contrast, the devices with the liquid-based electrolytes merely retained 50% of their original efficiency. The results showed that using gel-based electrolytes to fabricate DSSC devices can decrease the evaporation and leakage of liquid-based electrolytes, thereby extending the stability of such devices.

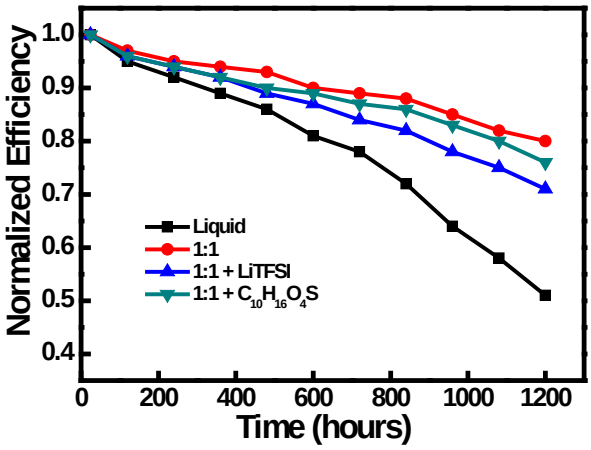

Fig.19. The stability of the DSSC devices with the gel-based and liquid-based electrolytes.

2.4. Conclusions

In this study, gel-based electrolytes were produced by mixing a liquid-based electrolyte with PMMA, which served as a gelator, to enhance the stability of the electrolytes and DSSC devices. PMMA demonstrates properties such as a low crystallization tendency, high material transmittance, and favorable conductivity and viscosity. Therefore, compared with conventional liquid-based DSSC devices, those made from PMMA gel-based electrolytes exhibit less electrolyte evaporation and leakage, thus achieving an extended stability. This study first fabricated DSSC devices by adopting gelator to electrolyte solution volume ratios of 1:0.5, 1:1, and 1:1.5. The properties of these gel-based electrolytes were then compared with those of the liquid-based electrolyte. According to the J–V, IPCE, and electrochemical impedance analyses, the DSSC with the 1:1 gel-based electrolyte exhibited the most satisfactory properties, obtaining a device efficiency of 6.75 %. Furthermore, 0.1 M LiTFSI and 0.1 M $C_{10}H_{16}O_4S$ were separately added to the gel-based electrolytes. An impedance spectrum analysis and conductivity testing of the simple-model devices showed that the added LiTFSI and $C_{10}H_{16}O_4S$ were effective in increasing the conductivity of the electrolytes. In addition, DSSC devices were fabricated with 1:1, 1:1 + LiTFSI, and 1:1 + $C_{10}H_{16}O_4S$ gel-based electrolytes. The properties of these devices were then compared with those of the devices with a liquid-based electrolyte through J–V, IPCE, and electrochemical impedance analyses. The results indicate that adding LiTFSI and $C_{10}H_{16}O_4S$ to the gel-based electrolytes effectively enhanced the device efficiency. In particular, the device with the 1:1+ LiTFSI gel-based electrolyte exhibited the optimal efficiency (7.28%), which was higher than that observed in the device with the liquid-based electrolyte. Another experiment also proved that the DSSC devices with the gel-based electrolytes exhibited a longer stability than did those using the liquid-based electrolyte. Therefore, using optimized gel-based electrolytes can enhance the power conversion efficiency and stability of DSSC devices.

3. Deposition of Tungsten oxide nanoparticles onto ITO

3.1. Introduction

We present an easy way to deposit a thin film of electro-chromic materials on the transparent, conducting glass of indium tin oxides (ITOs), suitable for mass-production. All the processes of material synthesis and deposition are carried out without using any vacuum systems. The WO_3 nanoparticles, used as electro-chromic materials, are synthesized in deionized water. They are then spray-deposited to generate a ~700-nm thick thin film on the ITO substrates. The as-prepared electro-chromic glass is put in the electrolyte of 0.1 M H_2SO_4. As an external voltage of ~±2.7 V is applied, the electro-chromic glass is switched alternatively between colored and bleached states. The colored state of the electro-chromic glass is blue and the transmission spectrum exhibits a blue-light peak centered at the wavelength of 440 nm. Light with wavelengths longer than 600 nm or shorter than 350 nm is reduced to be less than 10 %.

3.2 Experiment

Tungsten oxide (WO_3) nanoparticles were generated by electrical wire explosion process in deionized water. A tungsten wire of 0.3 mm in diameter was automatically fed to touch a counter electrode of a copper metal plate while a direct-current bias voltage of 48 V was supplied by a battery for the wire explosion. The peak value in electro-explosion was about 7.4 A in 2 s. The tungsten wire of 1 m in length was converted to WO_3 nanoparticles in de-ionized water (300 ml) in 20 min. The WO_3 nanoparticle suspension is light blue in color. The WO_3 nanoparticles were characterized by X-ray diffraction (XRD), transmission electron microscope (TEM), and scanning electron microscope (SEM). The nanoparticle suspension is

sprayed on ITO substrates heated at 200 ºC by using a home-made automatic spraying system. The thickness of the WO_3 nanoparticle film can be controlled and varied from several hundred nanometers up to several micrometers. To investigate electrochromic properties, the as-prepared electrochromic glass was put in electrolyte of 0.1 M H_2SO_4 acid solution and another ITO substrate was used as a counter electrode for applying a bias voltage of ~2.7 V. The electrochromic glass was switched alternatively between colored and bleached states. The transmittance of the colored state was measured with reference to its bleached state.

3.3. Results and Discussion

Fig. 20 shows the XRD spectrum with lattice planes indicated. It is clear that the WO_3 nanoparticles remain crystalline inside each one. The inset shows TEM image of WO_3 nanoparticles with a scale bar of 100 nm. The size of WO_3 nanoparticles is smaller than ~40 nm. The nanoparticles have wide size distribution from several nanometers up to 40 nanometers.

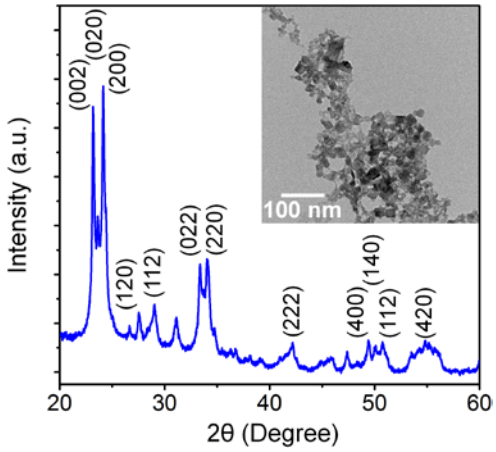

Fig. 20. XRD spectrum of WO_3 nanoparticle-assembled thin films with lattice planes indicated. The inset shows the TEM image of WO_3 nanoparticles.

The synthesized WO_3 nanoparticles are kept in the aqueous solution. The concentration of the WO_3 nanoparticles is about 0.02 M. The nanoparticle dispersion is used to spray on the ITO substrate which is heated at 200 ºC. It is about 40 min to prepare WO_3 nanoparticle film with a thickness of ~700 nm on an area of 5 cm by 5 cm. The as-deposited WO_3 nanoparticle thin film shows porous structure as shown in Fig. 21(a). The top-view SEM image shows network structures which are completely different from the original particle structures observed in TEM images. Fig. 21(b) presents the side-view image of the WO_3 nanoparticle thin film. The thickness is measured to be 676 nm.

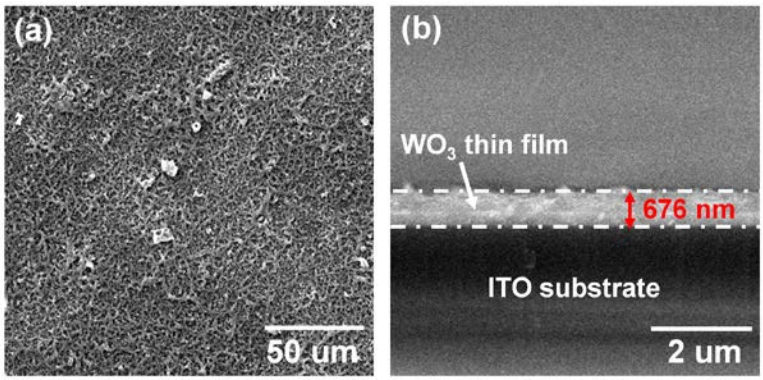

Fig. 21. (a) Top view SEM image of WO3 nanoparticle film on the ITO substrate. (b) Side view SEM image of WO3 nanoparticle film with a thickness of 676 nm on the ITO substrate.

The as-prepared electrochromic glass is put in an electrolyte for investigating its electrochromic properties. The colored and bleached states can be switched alternatively by ±2.7 V. Fig. 22 shows the transmittance of the colored state with reference to the bleached state of the electrochromic glass. It is noted that the colored state presents the transmittance with a peak centering at the wavelength of 440 nm. For the light of wavelength shorter than 350 nm, the transmitted light intensity is reduced to be less than one tenth of the incident light. On the other hand, for the wavelength longer than 600 nm, the light intensity reduction is more efficient. The transmitted light can be reduced to remain only several percent of its incident light strength. The WO_3 nanoparticle thin film shows high efficiencies in reducing the heat from the incident light.

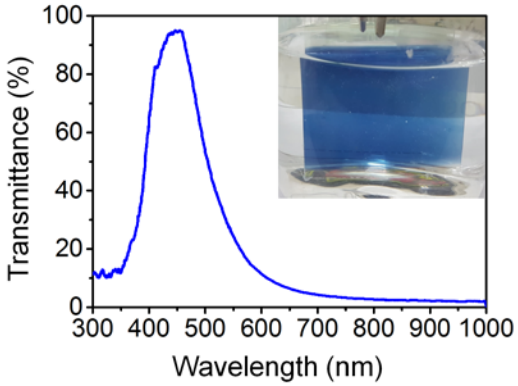

Fig. 22. Transmittance as a function of wavelength for the colored state of WO3 nanoparticle film on ITO glass after a bias voltage of ~2.7 V is supplied. The reference of the transmittance measurement is the bleached state of this electrochromic glass. The inset shows a photo of the colored state of a electrochromic glass with a size of 5 cm by 5 cm.

Electrical study of the graphene p-GaN contact interface for GaN UV LED applications

While Indium Tin Oxide (ITO) is the material of choice for transparent electrodes in the visible range, transmission drops significantly in the UV, making it undesirable for UV LED applications. Graphene, with much greater UV transmission, is an excellent alternative to ITO for UV LED applications. This fact is particularly true for p-type Gallium Nitride (pGaN), where achieving low contact resistance with transparent electrodes remains quite challenging [1]. Indeed, the graphene-pGaN [2] contact interface must be well understood to achieve a low contact resistance suitable for LED applications. Detailed electrical characterization of the graphene-pGaN contact has been performed to understand the underlying mechanisms governing the contact resistance and nature of the graphene-pGaN interface.

Four contact stacks to pGaN, including Ti(30nm)/Au(50nm), graphene(single layer)/Ti(30nm)/Au(50 nm), graphene(single layer)/Pt(100 nm), and Pt(100 nm), were fabricated in order to evaluate the graphene-pGaN contact interface. The low workfunction Ti and high workfunction Pt contacts without graphene served as control samples. Fig. 1 shows experimentally measured I-V characteristics of the four contact stacks to pGaN. The experimental data were fit by an analytical model for a forward biased Schottky contact in order to determine the effective barrier height for each contact stack. The barrier heights extracted from those fits are plotted in Figure 2 vs contact stack and in Figure 3 vs workfunction.

There are two key observations one can make giving insight into the underlying physics of the graphene-pGaN interface. First, the barrier height of the pGaN contact varies weakly with workfunction. This fact indicates that there are significant interface states which pin the barrier height and graphene does not alter these interface states. Therefore, effective

passivation of the pGaN surface is needed to allow low resistance graphene-pGaN contacts for UV LED applications. Second, the barrier height of the graphene-pGaN contact does not depend on the metal (Ti or Pt) on top of the graphene. This observation indicates that the graphene workfunction and the pGaN surface states determine the barrier height. Indeed, as seen in Figure 3, when the barrier height of the graphene contact is plotted against the graphene work function determined from Hall effect measurement, the graphene barrier height matches the trend established by the Ti and Pt control devices. Therefore, the graphene workfunction, not that of the top metal, controls the barrier height at the graphene-pGaN contact along with the pGaN surface states.

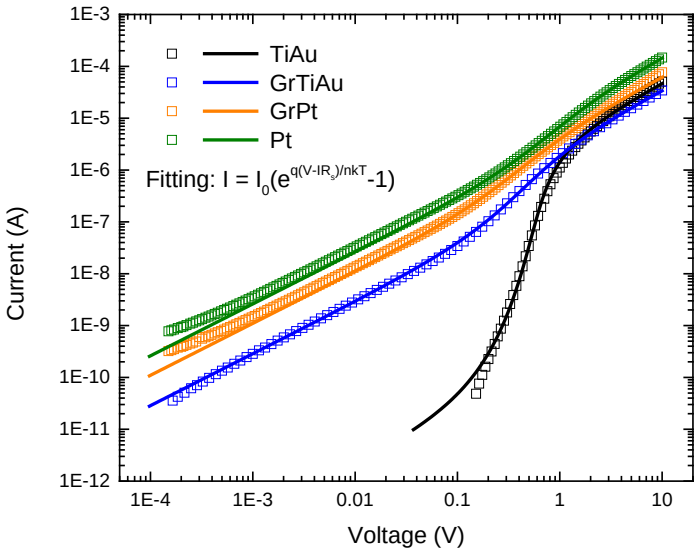

Fig . 1 .
Log-log plot of representative forward current vs. forward voltage for four different contact stacks on p-GaN. T he symbols are the measured data and the lines are fits using the equation noted in the figure.

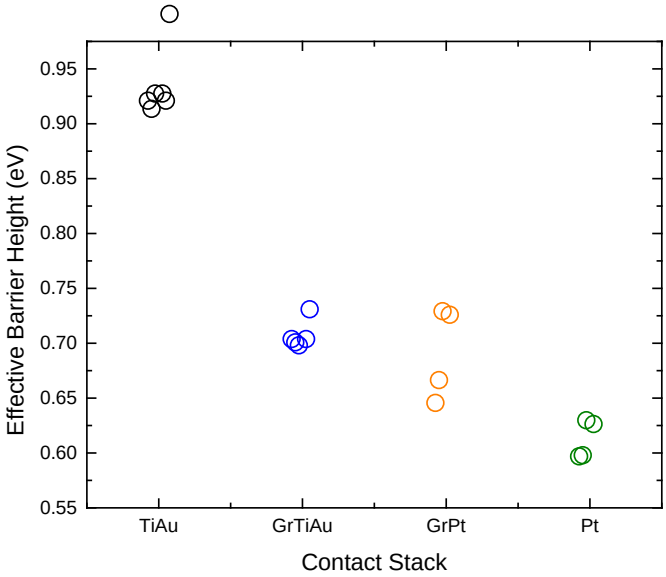

Fig. 2. Plot of the barrier height vs contact stack for p-GaN, determined from the I-V fittings from Figure 1 along with others not shown. Note that each symbol in the figure indicates a unique device.

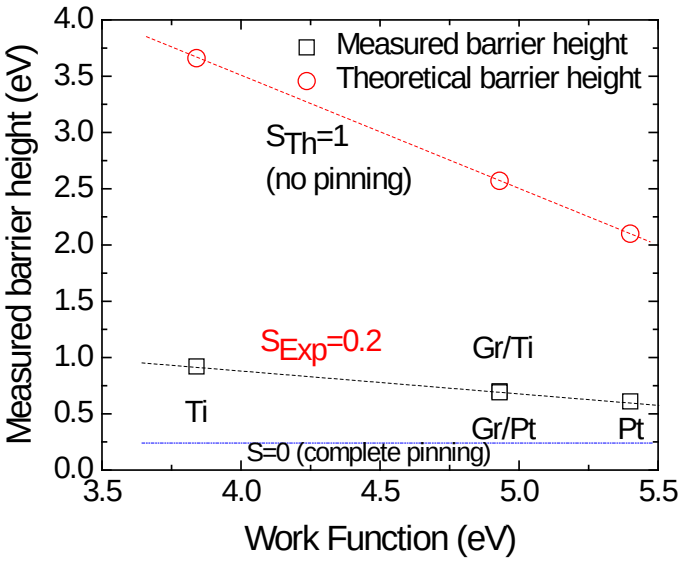

Fig. 3. Plot of the barrier height vs. workfunction of the contact material to p-GaN. The theoretical barrier heights calculated from the work function difference (Schottky Model) are pictured as red circles. The average barrier heights, calculated from those in Figure 2, are plotted as black squares. The slope of the barrier height vs. work function relationship, S, is experimentally determined to be 0.2, indicating that the barrier height is mostly pinned by interface states at the p-GaN contact, even when graphene is used.

References:

[1] J. O. Song, J.-S. Ha and T.-Y. Seong, "Ohmic-Contact Technology for GaN-Based Light-Emitting Diodes: Role of P-Type Contact," *IEEE Transactions on Electron Devices*, vol. 57, no. 1, pp. 42-59, 2010.

[2] L. Wang, W. Liu, Y. Zhang, Z.-H. Zhang, S. T. Tan, X. Yi, G. Wang, X. Sun, H. Zhu and H. V. Demir, "Graphene-based transparent conductive electrodes for GaN-based light emitting diodes: Challenges and countermeasures," *Nano Energy*, vol. 12, pp. 419-436, 2015.